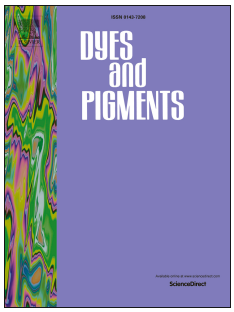

Pyrene-substituted cyclic triimidazole: An appealing and versatile luminescent scaffold for explosive detection

Matteo Formenti, Delia Blasi, Elena Cariati, Lucia Carlucci, Alessandra Forni, Clelia Giannini, Matteo Guidotti, Stefano Econdi, Daniele Malpicci, Daniele Marinotto, Elena Lucenti

PII: S0143-7208(22)00559-9

DOI: https://doi.org/10.1016/j.dyepig.2022.110637

Reference: DYPI 110637

To appear in: *Dyes and Pigments*

Received Date: 17 June 2022

Revised Date: 29 July 2022

Accepted Date: 1 August 2022

Please cite this article as: Formenti M, Blasi D, Cariati E, Carlucci L, Forni A, Giannini C, Guidotti M, Econdi S, Malpicci D, Marinotto D, Lucenti E, Pyrene-substituted cyclic triimidazole: An appealing and versatile luminescent scaffold for explosive detection, *Dyes and Pigments* (2022), doi: https://doi.org/10.1016/j.dyepig.2022.110637.

Author contribution statement

Matteo Formenti: Data Curation, Synthesis, Visualization, Writing - Original Draft, Writing - Review & Editing.

Delia Blasi: Data Curation.

Elena Cariati: Visualization, Writing - Original Draft, Writing - Review & Editing.

Lucia Carlucci: Visualization, Writing - Original Draft, Writing - Review & Editing.

Alessandra Forni: Visualization, Writing - Original Draft, Writing - Review & Editing.

Clelia Giannini: Data Curation.

Matteo Guidotti: Data Curation.

Stefano Econdi: Data Curation.

Daniele Malpicci: Data Curation, Synthesis.

Daniele Marinotto: Data Curation.

Elena Lucenti: Visualization, Writing - Original Draft, Writing - Review & Editing.

Pyrene-substituted cyclic triimidazole: an appealing and versatile luminescent scaffold for explosive detection

Matteo Formenti,[a] Delia Blasi,[a] Elena Cariati,[a,b,c] Lucia Carlucci,[a,c,*] Alessandra Forni,[b,c] Clelia Giannini,[a] Matteo Guidotti,[b] Stefano Econdi,[b] Daniele Malpicci,[a,b] Daniele Marinotto,[b] Elena Lucenti[b,c,*]

[a]*Department of Chemistry Università degli Studi di Milano, via Golgi 19, 20133 Milano (Italy)*
[b]*Institute of Chemical Sciences and Technologies "Giulio Natta" (SCITEC) of CNR, via Golgi 19, 20133 Milano (Italy)*
[c]*INSTM Research Unit of Milano, via Golgi 19, 20133 Milano (Italy)*

Two derivatives of cyclic triimidazole and pyrene, namely the blue emitting 3-(pyren-1-yl)triimidazo[1,2-*a*:1',2'-*c*:1",2"-*e*][1,3,5]triazine, **TTPyr**, and the yellow-orange emitting 11-(pyren-1-yl)triimidazo[1,2-*a*:1',2'-*c*:1",2"-*e*][1,3,5]triazine-3,7-dicarbaldehyde, **(CHO)$_2$TTPyr**, are here exploited for titration experiments with various nitroaromatic energetic hazardous materials and proposed as sensor species for the quantitative detection of explosives. The 565 nm fluorescence of **(CHO)$_2$TTPyr** represents a valid alternative to the **TTPyr** 420 nm one for analytes absorbing in the blue region. **(CHO)$_2$TTPyr** displays varying degrees of fluorescence quenching towards different nitroaromatics, among which picric acid (PA) detection has the highest sensitive response with a Stern-Volmer quenching constant value equal to 1.25×10^4 M^{-1} and a calculated detection limit of 0.63 ppm. From time resolved photoluminescence experiment, a static mechanism is recognized as responsible for the observed quenching. The hypothesis of a dark complex formation is supported through the isolation and characterization of a **TTPyr**/PA adduct with 2:1 stoichiometry.

1. Introduction

The current geopolitical instability in various parts of the world and the constant threat of criminal or terrorist acts with explosive devices calls for rapid and reliable detection methods capable to specifically detect low amounts of energetic hazardous chemicals and their precursors. In particular, military-grade 2,4,6-trinitrotoluene, TNT, is still widely utilized as a blasting agent not only in controlled explosions for peaceful purposes, but also in illicit activities, such as in improvised explosive devices, IEDs. Furthermore, TNT and its degradation by-products are persistent pollutants, recalcitrant to spontaneous self-decontamination, and often pose problems in terms of long-lasting pollution in sites in which large amounts of explosives have been used or dispersed. such as explosive manufacturing industrial facilities, obsolete arsenals, unexploded landmines, military proving grounds or areas where war combats took place [1,2]. For these reasons, a rapid, effective and reliable detection of explosives is constantly attracting attention as a tool to address these issues in terms of global security and environmental pollution hazard [3,4]. Along with TNT, other nitroaromatic compounds, NACs, such as 2,4-dinitrotoluene, DNT, or 2,4,6-trinitrophenol (also known as picric acid, PA) are common components of industrial explosives. Then, PA can be used as an explosive, as it more energetic than other analogous compounds [5,6], or as a component in dyes and pharmaceutical formulations [7].

In the search for low-cost and user-friendly sensors, the development of fluorescent compounds has emerged as a promising strategy due to the high sensitivity, selectivity, short response time, and the possibility to work both in solution and solid phase [8,9].

Triimidazo[1,2-*a*:1',2'-*c*:1",2"-*e*][1,3,5]triazine, **TT**, has been recently deeply investigated by us due to its fascinating luminescent behaviour comprising crystallization induced emission, CIE, and

ultralong room temperature phosphorescence, URTP, associated with π-π stacking interactions in the solid state [10–12]. Based on these, **TT** has been used as the central scaffold of a new family of full organic [13–20] and hybrid inorganic-organic [21–23] emitting materials. In particular, its monosubstituted pyrene derivative, 3-(1-pyren-yl)triimidazo[1,2-*a*:1',2'-*c*:1",2"-*e*][1,3,5]triazine, **TTPyr**, which crystallizes in different polymorphs, shows a very rich photophysics comprising excitation-dependent fluorescence and phosphorescence at ambient conditions, and mechanochromic and thermochromic behavior [20]. The partial conformational freedom of the Pyr moieties has been suggested as responsible for dual fluorescence in the solid state and for a broad blue fluorescence (at 420 nm) in DMSO solution. Moreover, the remarkably high quantum yield, Φ, equal to 90% measured in solution, much higher than that of pyrene itself (33.4%) in the same conditions, suggests that the TT moiety successfully suppresses the aggregation caused quenching, ACQ, phenomena affecting pyrene fluorescence [20–22]. Additionally, the material in aggregate-state has been successfully tested for cellular and bacterial imaging.

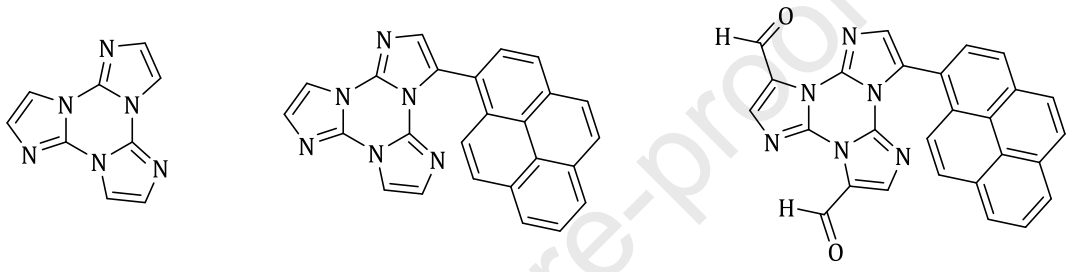

Figure 1. Chemical structures of **TT** and its derivatives used as probes in the present work.

It has been extensively shown that the pyrene moiety is a powerful building block to assemble molecules [24–33], polymers [34], nanoaggregates [35–37] and 2D [38] or 3D [39,40] structures for sensing of nitroaromatic compounds. This feature arises from π-π stacking between electron rich pyrene and electron poor nitroaromatics [24–28,30,34–39,41–43].

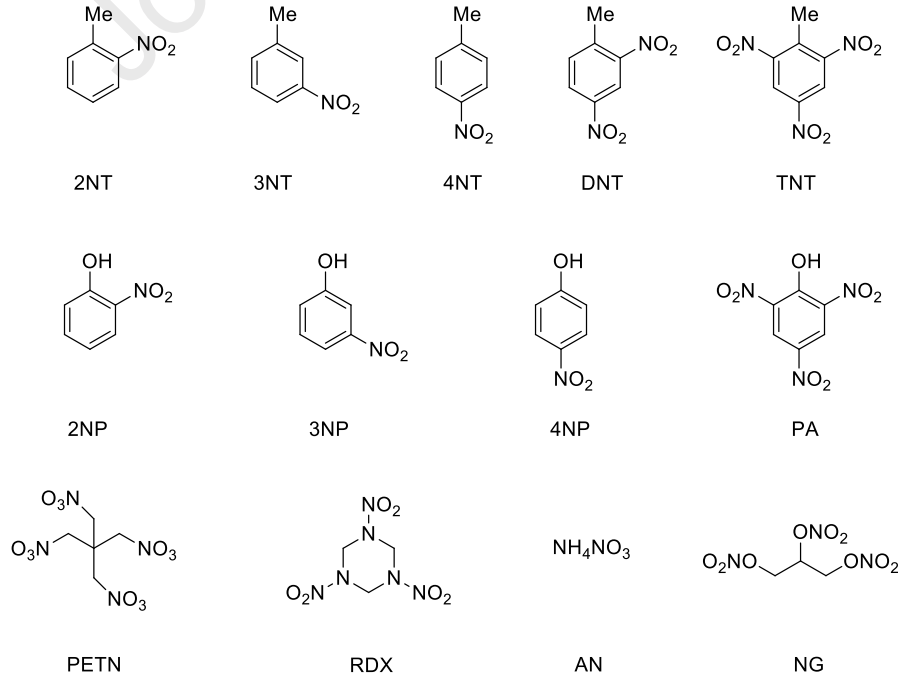

Figure 2. List of explosives tested in the present work.

Based on the high emissive performance of **TTPyr** [20], we have therefore decided to investigate this compound and its unprecedented orange emitting analogue, 11-(pyren-1-yl)triimidazo[1,2-*a*:1',2'-*c*:1",2"-*e*][1,3,5]triazine-3,7-dicarbaldehyde, **(CHO)$_2$TTPyr** (see Figure 1), as single-molecule fluorescent probes for explosives.

Performances of the two sensors have been investigated by means of fluorescence-quenching titrations through the incremental addition of analytes to 1.0x10^{-5} M DMSO solutions of **TTPyr** and **(CHO)$_2$TTPyr**. A large number of highly energetic molecules and explosives has been tested (see Figure 2), comprising various nitrotoluenes and nitrophenols, ammonium nitrate, AN, pentaerythritol tetranitrate, PETN, cyclotrimethylentriamine, RDX, in the form of plastic explosive C4 and nitro-glycerine, NG, in the form of dynamite.

The orange emission of **(CHO)$_2$TTPyr** in DMSO represents a valid alternative to the blue one of **TTPyr** for explosives with absorption in the blue region. Time resolved emission spectroscopy has been used to establish a static quenching mechanism in the observed sensing process.

2. Results and Discussion

As previously reported [20], diluted DMSO solutions of **TTPyr** (10^{-5}–10^{-6} M) show at room temperature, RT, two absorption bands with replicas at 257, 268, 279 nm and 332, 347 nm, both with main pyrene character as supported by theoretical and experimental evidences, and an intense very broad fluorescent emission at 420 nm (absolute quantum yield, Φ, equal to 92%) (Figure 3). Based on theoretical calculations, such emission was assigned to deactivation from two S_1 states associated with two different, almost isoenergetic (Δ=0.6 kcal/mol) conformations of **TTPyr** possibly present in solution [20].

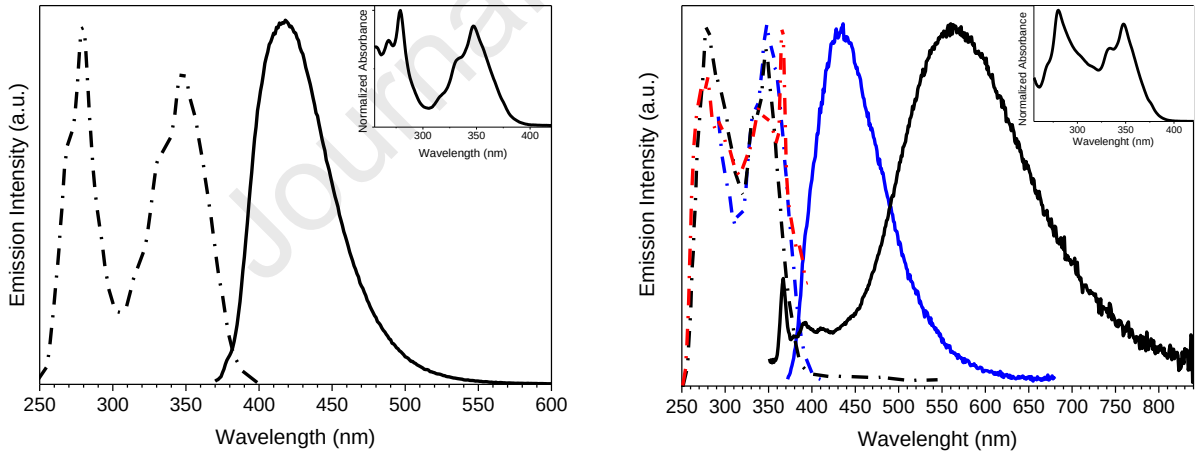

Figure 3. Normalized excitation (dashed-dotted line) and emission (continuous line) spectra. Left: **TTPyr** in DMSO (1.0x10^{-5} M; λ_{em} = 420 nm and λ_{exc} = 350 nm); inset, normalized absorption spectra in DMSO; right: **(CHO)$_2$TTPyr** 1.0x10^{-5} M in toluene (blue lines, λ_{em} = 420 nm, λ_{ex} = 350 nm) and DMSO (λ_{em} = 565 (black line) and 412 nm (red line), λ_{exc} = 330 nm); sharp peaks at 364 and 367 nm in the excitation and emission spectrum, respectively, are Raman bands of DMSO; inset, normalized absorption spectra in DMSO.

Incremental addition of NACs (nitrophenols and toluenes) to DMSO solutions of **TTPyr** (1.0x10^{-5} M) results in a strong attenuation of the intensity of the bright blue fluorescence at 420 nm as reported in Figure 4a (where TNT is reported as an exemplar) and Figures S6-S14. The intensity quenching ability follows the order: PA > 4NP > 2NP > 3NP > TNT > DNT >3NT ≅ 2NT >4NT, with attenuation

in the 98 - 18 % range in the presence of 50 eq of explosive (see Figures S6-S14). On the other side, negligible effects on the emission intensity are observed in the presence of aliphatic and inorganic energetic molecules (NG, PETN, RDX and AN) (see Figure 4b, where NG is reported as an exemplar, and Figures S15-S18).

Quenching experiments performed by using nitrophenols result in anomalous emission features as reported in Figure 4c for 4NP (see also Figures S11-S14). This phenomenon can be explained by the fact that the 420 nm emission of **TTPyr** is affected by the well-known secondary inner filter effect [36] in the presence of energetic compounds absorbing in the blue region (4NP, with absorption maxima at 435 nm and all the other nitrophenols, see Figure 4c where the absorption spectrum of 4NP is superimposed to the emission of **TTPyr**).

Therefore, caution has to be used when dealing with data collected for such analytes for which evaluation of the interaction strength can be performed only in spectral regions where their absorptions do not overlap with **TTPyr** emission.

Fluorescence quenching titrations have been analysed through the Stern–Volmer (SV) equation (see Table 1 and Figures 4d and S19), $I_0/I = 1 + K_{SV}[Q]$, where I_0 and I are emission intensities before and after addition of the quencher, respectively, [Q] is the quencher concentration and K_{SV} is the Stern-Volmer constant (M^{-1}), a parameter that allows to determine the strength of the quenching interactions and that can be extracted by plotting I_0/I vs [Q]. For most of the analytes, SV plots have been determined at the emission maximum (420 nm), however, due to inner filter artefacts, data for nitrophenols have been calculated at lower sensitivity points (at 490 nm for PA, 2NP and 3NP and at 500 nm for 4NP). For all analytes, SV plots result in a linear relationship with an upward curvature only for nitrophenols at high concentrations where the intensity of the emission signal is too low and results in instrumental artefacts (see Figure 4d).

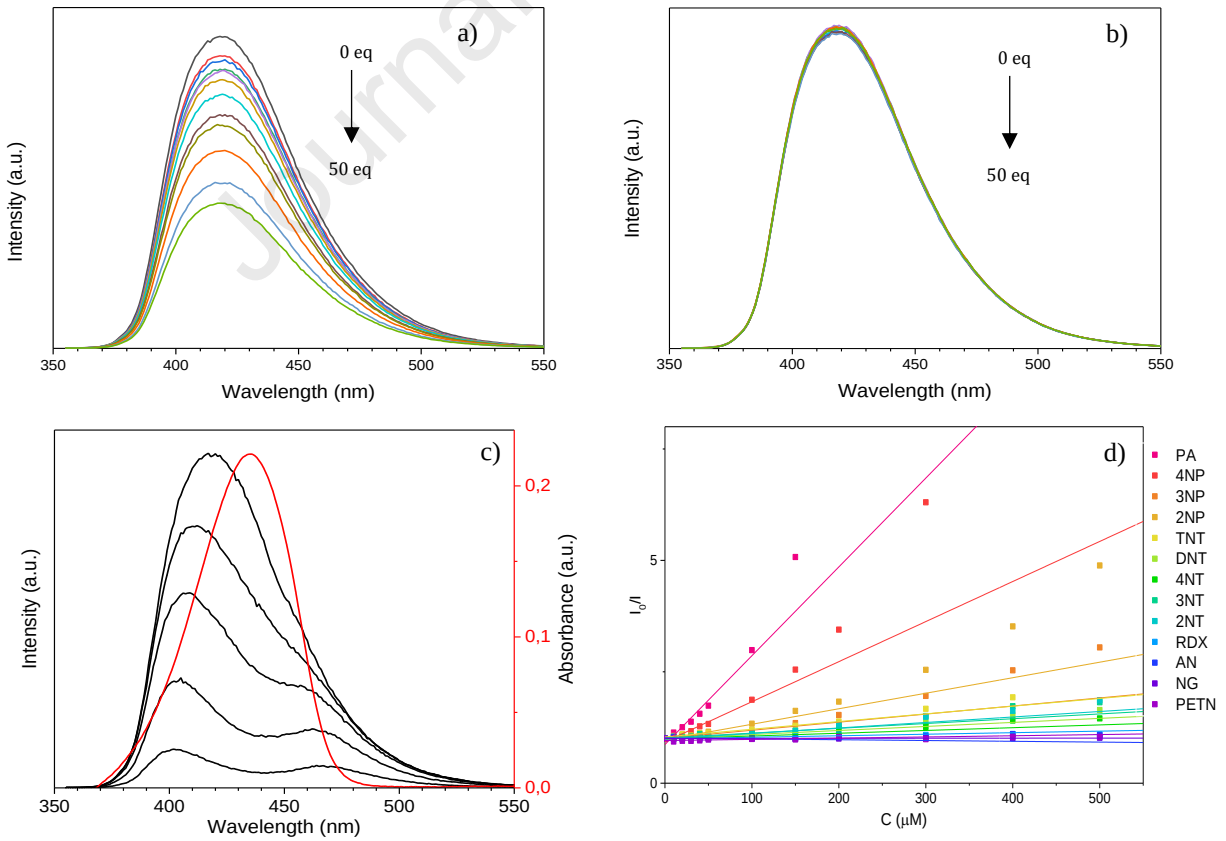

Figure 4. a) Quenching of **TTPyr** emission by TNT: spectra collected by exciting at 350 nm the $1.0x10^{-5}$ M DMSO solution of **TTPyr** starting from 0 (black line) up to 50 equivalents of TNT (green line); b) emission spectra (λ_{exc} = 350 nm) of $1.0x10^{-5}$ M DMSO solutions of **TTPyr** without and with increasing amount (up to 50 equivalents) of NG; c) solid lines: emission spectra (excitation wavelength 350 nm) of $1.0x10^{-5}$ M DMSO solutions of **TTPyr** without and with increasing amount (up to 20 equivalents) of 4NP. Red line: absorption spectrum of 4NP ($1.0x10^{-5}$ M) in DMSO; d) Stern-Volmer plots of **TTPyr** with explosives.

In order to check for a possible solvent effect on quenching experiments, solutions of **TTPyr** with TNT in DMSO/water (v/v%: 99/1; 80/20; 70/30; 50/50) have been performed to be compared with DMSO itself, where a K_{SV} of 2170 was determined.
As previously reported [20], the addition of water up to 50% to DMSO solutions of **TTPyr** results in a slight intensification of the emission and a concomitant blue shift from 420 to 410 nm. Moreover, the quenching effectiveness shows a drastic decrease at 1% water (K_{SV} from 2170 at 0% to 1000 M^{-1}) and a smoother trend at higher water content (780, 700 and 460 M^{-1} at 20, 30 and 50%, respectively) (see Figures S20-S23). This observation is compatible with water/**TTPyr** specific interactions in addition to solvation effect.
Further investigations in THF using PA and TNT (see Figures S24 and S25) revealed a strong attenuation of the capability of both analytes to quench **TTPyr** emission. This is particularly relevant for TNT with respect to PA (from 2170 in DMSO to 470 M^{-1} for TNT, from 14600 to 8380 M^{-1} for PA), indicating the importance of solvating effect on both partners of the quenching experiment.

To overcome the limitation of **TTPyr** as sensor for nitrophenols, the possible, alternative use of **$(CHO)_2$TTPyr** has been investigated. This new compound has been synthesized by lithiation of **TTPyr** with *n*-butyllithium followed by nucleophilic addition on DMF and characterized by NMR and mass spectroscopy (see the Experimental Section). Differently from the essentially apolar character of **TTPyr** (dipole moment computed in DMSO, μ_{DMSO}, equal to 1.12 D), **$(CHO)_2$TTPyr** is a compound of medium polarity (μ_{DMSO} = 5.88 D) due to the presence of the electron-acceptor carbonyl groups. Its electrostatic potential, plotted on the isodensity surface of electron density, shows a region of negative potential localized on pyrene (see inset of Figure 5). Comparison of the electrostatic potential map of **$(CHO)_2$TTPyr** with that of **TTPyr** (see Figure S48) evidence, for the latter compound, a much more extended negative area on pyrene, characterized by higher (in magnitude) values (maxima on the pyrene envelop are –0.065 and –0.046 a.u. for **TTPyr** and **$(CHO)_2$TTPyr**, respectively).

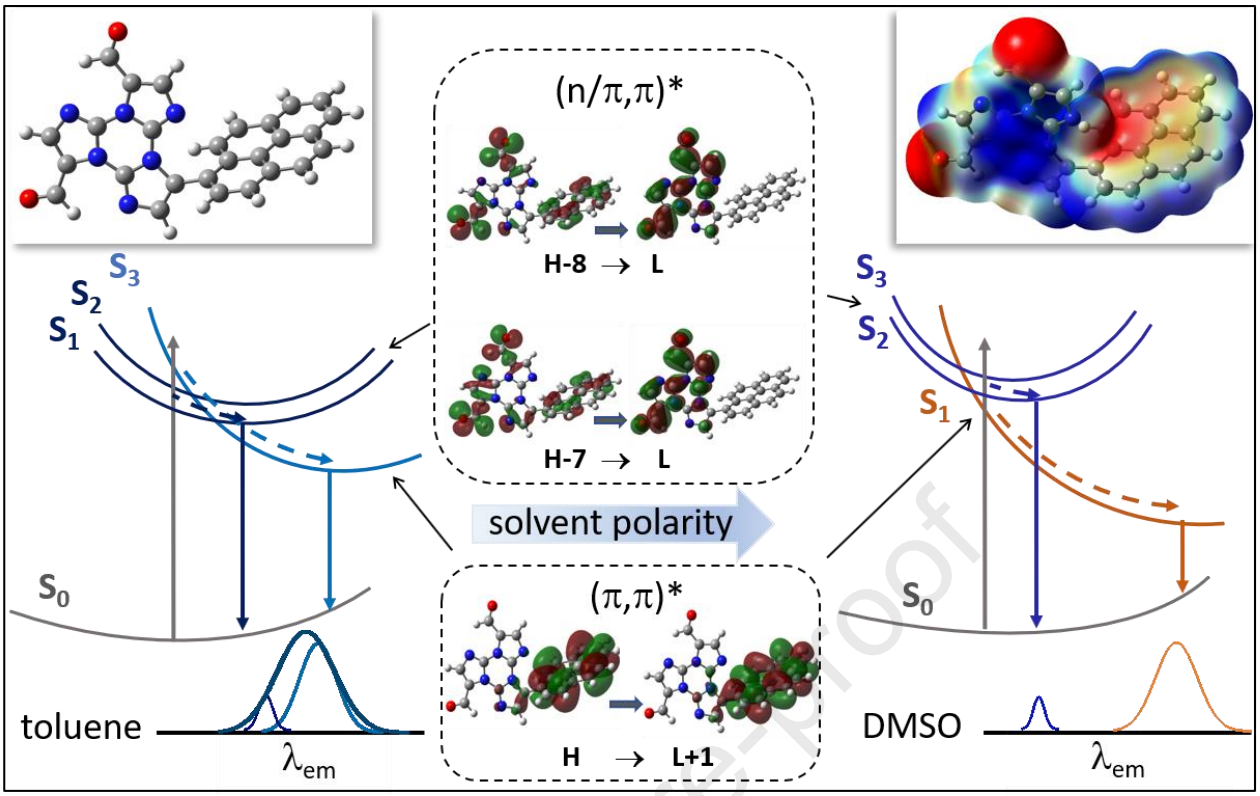

Figure 5. Schematic representation of the low energy absorption and emissions of **(CHO)$_2$TTPyr** in toluene (left) and DMSO (right), together with plots of the orbitals mainly involved in the excitations in DMSO (very similar plots are obtained in toluene). In the insets, DMSO optimized geometry (left) and electrostatic potential (right), mapped on the isosurface (0.001 a.u.) of electron density. Values of electrostatic potential range from -0.025 (red) to 0.025 (blue) a.u.

Diluted (1.0x10^{-5} M) DMSO solutions of **(CHO)$_2$TTPyr** are characterized by two absorption bands with peaks at 270 (sh), 280 nm and 333, 348 nm (assigned to (π,π*) transitions mainly localized on the (CHO)$_2$TT and pyr moieties, respectively, see below) and a broad fluorescence centered at 565 nm, together with a weak structured fluorescence at 392, 410 nm (absolute quantum yield, Φ, equal to 3%, τ_{av} = 2.76 ns). Interestingly, toluene solutions (1.0x10^{-5} M) of **(CHO)$_2$TTPyr**, though showing an absorption spectrum almost overlapped with that in DMSO, display a narrower and blue-shifted fluorescent emission at 436 nm (Φ = 5%, see Figure 3 right).
DFT and TDDFT calculations on **(CHO)$_2$TTPyr**, performed in both DMSO and toluene, provide a simulated absorption spectrum (Figure S49) with two main bands separated by about 0.90 eV, in agreement with the observed one though shifted at slightly higher energy. These two bands result from convolution of more transitions, among which the more intense ones (i.e. characterized by large oscillator strength, *f*) have (π,π*) character and are localized on pyrene (low energy band) and mostly on (CHO)$_2$TT (high energy band). Focusing on the region at low energy (see Figure 5 and Tables S2-S4), three almost overlapped states are computed at about 310 nm in both solvents, that is the strong (π,π*) one and two almost silent ($f \sim 0$) states, possessing mixed (n/π,π*) character with strong CHO contribution (see Figures S50 and S51 for plots of the frontier MOs in DMSO and toluene, respectively). With the aim of exploring the nature of the emissive states in the two solvents, geometries of the (π,π*) and the lower energy (n/π,π*) excited states have been optimized in DMSO and toluene along their own potential energy surface (see Table S2). In DMSO (see Figure 5, right),

the (π,π*) state undergoes a large electronic rearrangement associated with increased intramolecular conjugation and large red shift of the relaxed state, computed at 412 nm. The (n/π,π*) relaxed geometry, instead, remains nearly unvaried with respect to the ground state one and lies at much higher energy, 343 nm. Contrarily, in toluene (see Figure 5, left) a reduced red shift is obtained for the relaxed (π,π*) state, computed at 390 nm, while the (n/π,π*) one lies at 356 nm. It is therefore hypothesised that the different character of the two emissive states makes dual fluorescence possible. In DMSO, their large energy separation (about 0.9 eV) allows both states to be experimentally detected, with a considerably higher intensity of the (π,π*) transition compared with the weakly allowed (n/π,π*) one. On the other hand, in toluene the two emissive states are too close and only the predominant (π,π*) emission is observed. The decreasing in Φ on going from toluene to DMSO agrees with the energy gap law predicting a more competitive internal conversion in the latter solvent.
The red-shifted fluorescence of **(CHO)$_2$TTPyr** is, of course, not prone to be absorbed by nitrophenols and, therefore, represents a good alternative to **TTPyr** in such cases. DMSO solutions of **(CHO)$_2$TTPyr** have been tested for the full range of highly energetic compounds and explosives and SV plots have been determined at the emission maximum (565 nm), giving results that are very similar, also for nitrophenols, to the ones calculated for **TTPyr** (see Table 1 and Figures S28-S41).

	TTPyr		**(CHO)$_2$TTPyr**	
Explosive	**K_{SV} (M^{-1})**	**LOD (μM)**	**K_{SV} (M^{-1})**	**LOD (μM)**
RDX	2.30E+02	113	1.66E+02	164
PETN	1.74E+02	114	-1.15E+01	/
NG (dynamite)	2.00E+02	126	2.17E+01	880
AN	1.89E+02	120	1.54E+02	146
2NT	1.71E+03	18.15	4.70E+02	41.62
3NT	2.57E+03	17.00	5.34E+02	30.50
4NT	9.75E+02	28.41	5.79E+02	29.57
DNT	1.31E+03	18.46	1.06E+03	31.76
TNT	2.17E+03	8.20	1.45E+03	10.27
2NP	3.48E+03	12.56	4.86E+03	3.66
3NP	1.81E+03	24.13	4.90E+03	7.58
4NP	8.99E+03	4.87	1.12E+04	2.53
PA	1.46E+04	2.85	1.25E+04	2.76

Table 1. List of the Stern-Volmer constants and LODs obtained on intensity data at 420 nm for **TTPyr** and 565 nm for **(CHO)$_2$TTPyr**, (λ_{exc} = 350 nm). For the data set of **TTPyr** with PA, 3NP and 2NP data are calculated on the emission intensity at 490 nm while for 4NP at 500 nm in order to minimize secondary inner filter effect.

From data reported in Table 1, it can also be inferred that non-NACs explosives possess much lower quenching constants than NACs. For **(CHO)$_2$TTPyr** probe, the weakly negative constant of PETN can be explained with a substantially null interaction. Moreover, an almost 10 times stronger interaction with nitrophenols with respect to nitrotoluenes can be observed. PA is characterized by the strongest interaction with a K_{SV} equal to 1.46×10^4 M^{-1} with **TTPyr** and 1.25×10^4 with **(CHO)$_2$TTPyr**. These results support the use of cyclic triimidazole derivatives as selective NACs sensors. Photographs of 1.0×10^{-5} M solutions of **TTPyr** and **(CHO)$_2$TTPyr** in the presence of different amounts of PA are shown in Figure 6, where the corresponding quenching phenomena are more clearly visualized.

Limits of detection, LODs, in the order of magnitude of μM, reported in Table 1, have been calculated with the 3σ method [44], where LOD=3σ/K with σ being the I_0/I_0 error calculated from standard deviation of the blank and K the K_{SV} (see the Experimental Section). Calculated LODs are in line with the ones obtained with other pyrene functionalized explosive sensors [24].

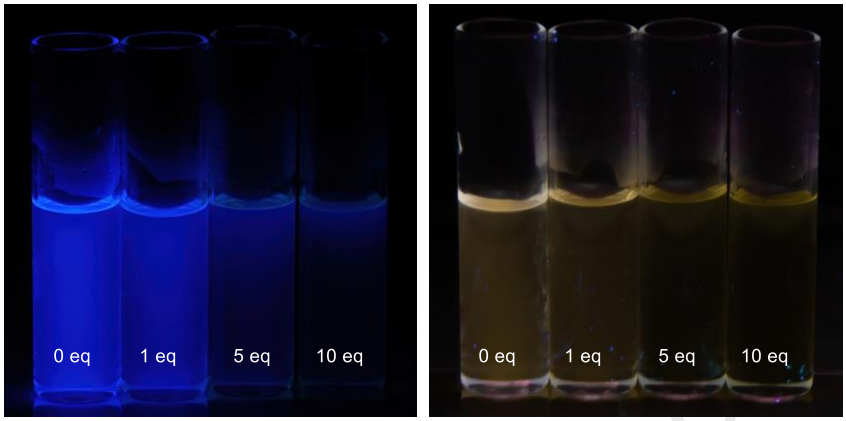

Figure 6. The effect of PA (0; 1.0; 5.0; 10.0 $x10^{-5}$ M from left to right) on the emission of $1.0x10^{-5}$ M **TTPyr** (left) and $1.0x10^{-5}$ M **$(CHO)_2$TTPyr** (right). Photographs are taken under a 366 nm UV irradiation.

Once established the effectiveness of **TTPyr** and **$(CHO)_2$TTPyr** as sensors for energetic materials and explosives, the mechanism involved in the quenching phenomenon has been investigated. It is well known that in static quenching, sensor-analyte interaction occurs in the ground state and results in a non-emissive or differently emissive complex formation. In this case, only uncomplexed sensor molecules do radiatively decay after excitation at the fixed emission wavelength with unperturbed lifetime. In dynamic quenching, on the other side, interaction involves sensor molecule in the excited state so that the encounter results in reduced excited state lifetime. Therefore, to discriminate between

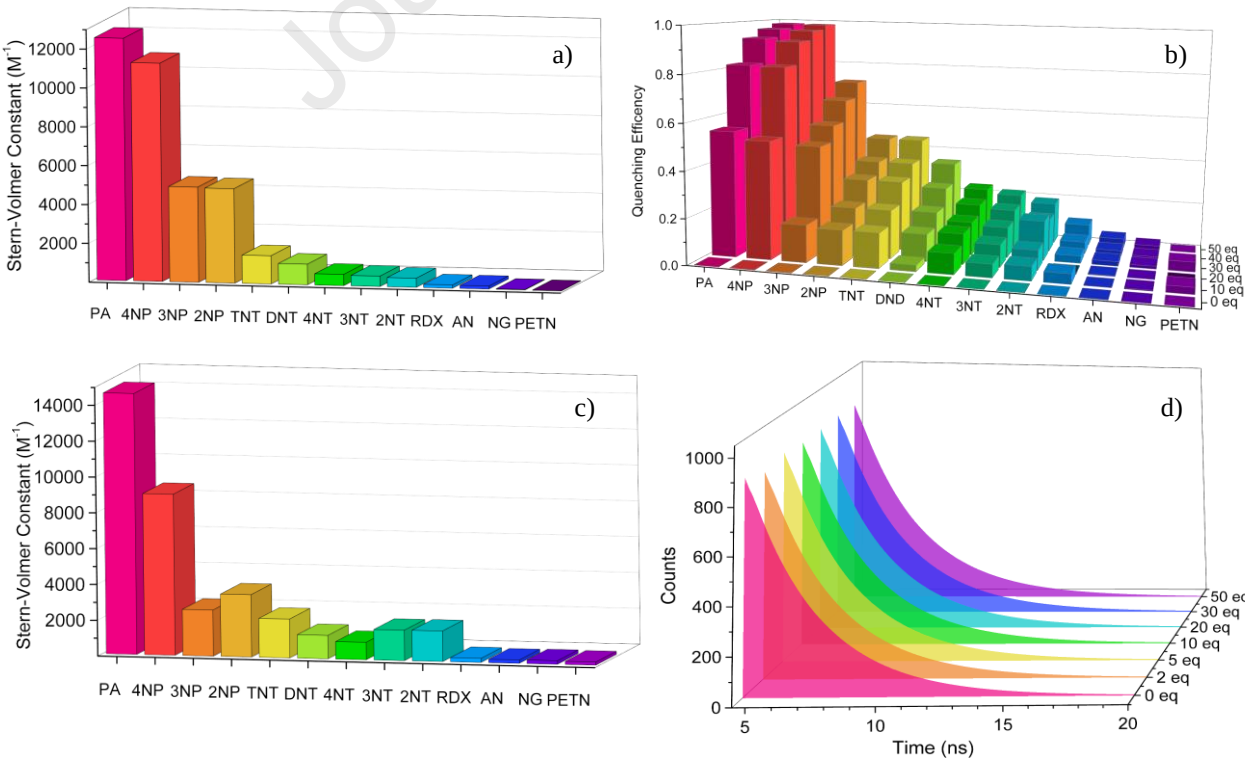

static

Figure 7. a) Stern-Volmer constants, K_{SV}, of **(CHO)$_2$TTPyr** with explosives; b) **(CHO)$_2$TTPyr** emission quenching efficiency of explosives at various concentrations (0, 10, 20, 30, 40 and 50 equivalents); c) Stern-Volmer constants, K_{SV}, of **TTPyr** with energetic materials; d) decay curves of **TTPyr** at different concentration of TNT showing no change in experimental lifetime.

(ground state complex formation) and dynamic quenching, time-resolved measurements have been performed on **TTPyr** (selected for its higher emission signal) in DMSO ($1.0x10^{-5}$ M) in the absence and in the presence of increasing concentration of PA or TNT, chosen as exemplar analytes for their high binding affinities with the sensor.

These experiments reveal constant excited state lifetime (τ_{av}, 2.76 ns) even at very high quencher concentration (up to 500 μM for TNT, 50 eq, see Figures 7d and S27, and 100 μM, 10 eq, for PA, see Figure S26). At PA concentration higher than 100 μM, the intensity of the emission signal was too low for the instrumental sensitivity. Such behaviour suggests the formation of non-emissive supramolecular adducts (dark complexes) between the fluorophore and the quenchers whose formation constants correspond to the K_{SV} of I_0/I vs [Q] plots.

UV-vis absorption titration experiments performed on **TTPyr** in the presence of PA in DMSO solutions do not reveal any fingerprint of a possible ground-state analyte/sensor complex (see Figures S44 and S45). However, the formation of a complex was supported by ^{1}H-NMR spectra and elemental analysis experiments on a red powder precipitated from a **TTPyr**/PA acetonitrile (ACN) solution (see Figures S4 and S5). Such measurements unequivocally indicate a **TTPyr**:PA = 2:1 stoichiometry (CHN composition, calculated: 65.6% C; 3.1% H; 20.5% N; found: 65.7% C; 3.3% H; 20.4% N) ^{1}H-NMR spectra led not only to a better definition of the adduct, but also to unquestionably exclude any analyte-sensor chemical reaction, hence giving the possibility to use **TTPyr** derivatives as reusable sensors. Remarkably, a sensor-analyte 2:1 stoichiometry has been obtained through a Job's plot via fluorimetric analysis (Figure 8). Job's plots of **TTPyr** with TNT and **(CHO)$_2$TTPyr** with PA (see Figures S42-S43) suggest different stoichiometries, however the 2:1 stoichiometry of the **TTPyr**/PA adduct has been confirmed by single crystal X-ray diffraction analysis performed on small crystals precipitated from an ACN **TTPyr**/PA (2/1) concentrated solution. Experimental details of single crystal X-ray diffraction analysis are given in the Experimental Section, crystal data, collection data and refinement details are reported in Table S1. Comparison between calculated and experimental XRPD patterns is shown in Figure S46.

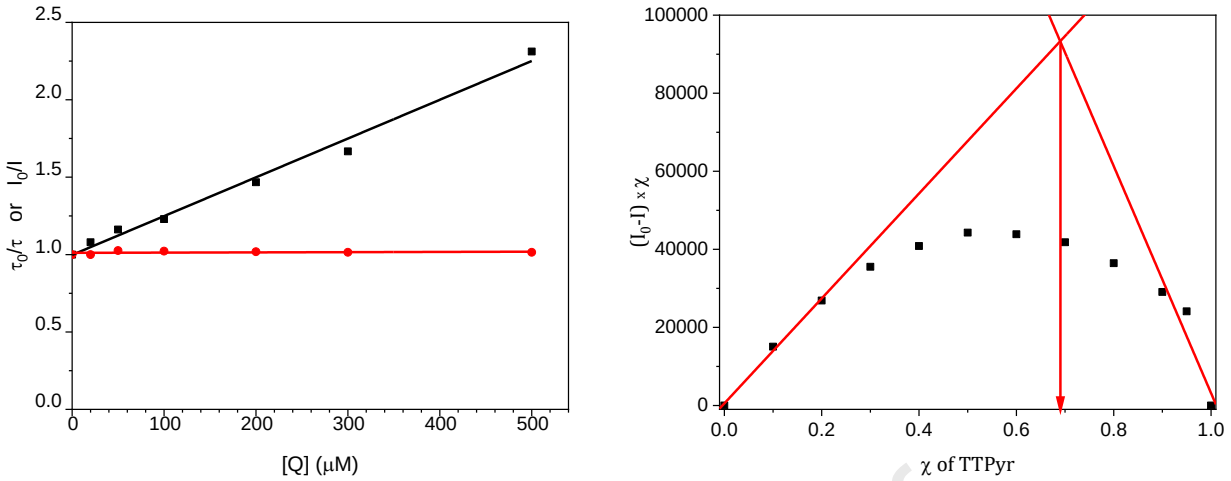

Figure 8. Left: Stern-Volmer plot of **TTPyr** quenched by TNT. Black line from intensity; red line from lifetime. Right: Job's plot for the interactions between **TTPyr** and PA. χ is the molar fraction of **TTPyr** [45].

The asymmetric unit of the crystal structure of **TTPyr**/PA co-crystal contains three molecules interacting through hydrogen bond and π-π stacking (Figure 9). Crystal packing analysis shows the formation of columnar aggregates displaying the ···**TTPyr**···PA···**TTPyr**···**TTPyr**···PA···**TTPyr**··· sequence (see Figure S47). Stacking interactions involving the π-electron systems of pyrene and PA are established within the aggregate, while the TT unit protrude on the same side of the column. Very short distances (3.415 and 3.517 Å) are found between the geometric centroids (Cg) of pyrene and PA benzene ring, as a consequence of the opposite electronic nature of the interacting aromatic systems: a donor one for pyrene, as evidenced by the electrostatic potential map of **TTPyr** (Figure 5), and an acceptor one for PA, due to the electron-acceptor nitro substituents. In addition, the much larger negative area of electrostatic potential of **TTPyr** compared to **(CHO)$_2$TTPyr** (Figure S48) suggests a stronger interaction within the **TTPyr**/PA adduct with respect to the **(CHO)$_2$TTPyr**/PA one, explaining the higher performance of the former for the detection of compounds of the NT series (see Table 1). Longer Cg···Cg distances (4.046 Å) are found between adjacent pyrene rings along the columnar aggregate, whose bonded TT units are themselves involved in π-π stacking interactions, with triazinic centroids distance equal to 4.365 Å.

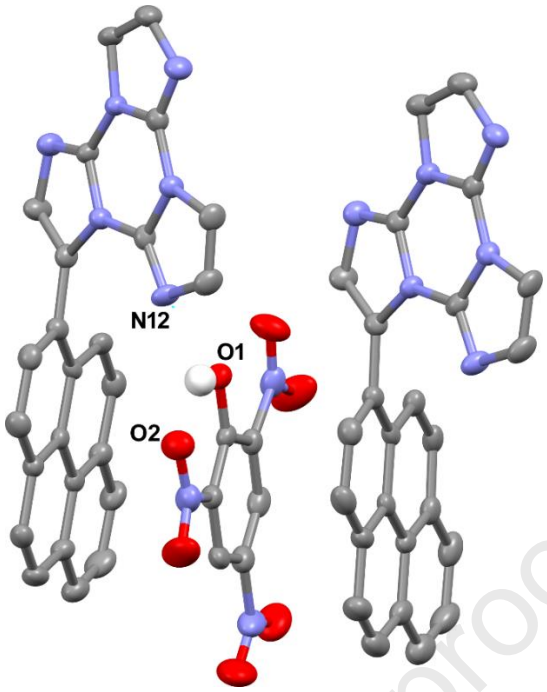

Figure 9: View of the asymmetric unit of the crystal structure of **TTPyr**/PA containing one PA and two **TTPyr** molecules. The three molecules are involved in bifurcated hydrogen bond between the hydroxyl hydrogen of PA and O2 (intramolecular, O1···O2 = 2.601(5) Å) and N12 (intermolecular, O1···N12 = 2.879(5) Å) atoms, and in **TTPyr**…PA…**TTPyr** stacking interactions. Hydrogen atoms, except the hydroxyl one, are omitted for clarity, ellipsoids are drawn at 30% of probability level.

3. Conclusions

Pyrene chromophoric performances can be enhanced through functionalization with cyclic triimidazole opening to a new family of sensors for highly energetic and explosive compounds based on fluorescence quenching. The sensor-analyte interaction, measured through Stern-Volmer analysis, increases in the order: aliphatic and inorganic explosives < nitrotoluenes < nitrophenols, resulting in the strongest response in the presence of PA. Time resolved studies suggest a static quenching mechanism for NACs and, in the case of **TTPyr**/PA, the corresponding dark complex with 2:1 stoichiometry has been isolated and characterized. The presence of aldehydic groups in **(CHO)$_2$TTPyr** results in dual emission in DMSO originated from (π,π*) and (n,π*) states with the former strongly red-shifted with respect to **TTPyr**. Such a feature allows to overcome inner filter effects observed for nitrophenols.

4. Experimental Section

4.1. General information

All reagents were purchased from chemical suppliers and used without further purification. Triimidazo[1,2-a:1',2'-c:1",2"-e][1,3,5]triazine, **TT** [46], its monobromo and monopyrene derivatives (namely 3-bromotriimidazo[1,2-a:1',2'-c:1",2"-e][1,3,5]triazine, **TTBr** [19], and 3-(1-pyren-yl)triimidazo[1,2-a:1',2'-c:1",2"-e][1,3,5]triazine, **TTPyr** [20]) were prepared according to literature procedures. Highly energetic compounds and explosives here tested (TNT, NG, PETN, RDX) were obtained, as military-grade reference samples in sub-hazardous amounts, from Italian law enforcement agencies. TNT was purified by two-step re-crystallization, first from hot benzene, then from 95% ethanol as described in [47]. PA was previously stored under water and was carefully dried *in vacuo* at room temperature prior to use.

WARNING: TNT, NG, PETN, RDX and PA are highly energetic materials and are very sensitive to mechanical and thermal shocks and friction. These substances must thus be handled with extreme caution, in very low amounts.

^{1}H and ^{13}C NMR spectra were recorded on a Bruker AVANCE-400 instrument (400 MHz). Chemical shifts are reported in parts per million (ppm) and are referenced to the residual solvent peak (DMSO, ^{1}H 2.50 ppm, ^{13}C 39.5 ppm). Peak multiplicities are described in the following way: s, singlet; m, multiplet.

Mass spectra were recorded on a Thermo Fisher (Thermo Fisher Scientific, Waltham, MA USA) LCQ Fleet Ion Trap Mass Spectrometer equipped with UltiMate™ 3000 HPLC system. UV-Visible spectra were collected by UV-3600i Plus UV-VIS-NIR Spectrophotometer (Shimadzu Italia S.r.l., Milan, Italy). Steady state emission and excitation spectra were obtained using a FluoroLog 3 (Horiba UK Limited, Northampton, United Kingdom) spectrofluorometer. The steady state measurements were recorded by a 450 W Xenon arc lamp. Photoluminescence quantum yields were measured using a C11347 Quantaurus–Absolute Photoluminescence Quantum Yield Spectrometer (Hamamatsu Photonics K.K), equipped with a 150 W Xenon lamp, an integrating sphere and a multichannel detector. Photoluminescence lifetime measurements were performed on a FLS 980 (Edinburgh Instrument Ltd., Livingston, United Kingdom) spectrofluorometer using Edinburgh Picosecond Pulsed Diode Laser EPL-375 (Edinburg Instrument Ltd.) with data acquisition devices time correlated single-photon counting (TCSPC).

The data needed to calculate the quenching intensity were acquired on solutions $1.0x10^{-5}$ M in sensor and with increasing concentration of analyte, from 0 M to $5.0x10^{-4}$ M, with the following parameters: excitation wavelength 350 nm; emission acquisition from 370 nm to 680 nm, step 1 nm; integration time 0.3 s. **TTPyr** emission maximum is 420 nm, **$(CHO)_2$TTPyr** emission maximum is 535 nm.

In the 3σ method used to calculate LODs (LOD=3σ/K) [44], σ is the I_0/I_0 error obtained by the standard deviation calculated from 60 points acquired at the fluorophore emission maxima in the same conditions used for quenching titration experiments. The obtained K_{sv} from Stern-Volmer plots is then taken as K.

4.2. Synthesis

Synthesis of 11-(pyren-1-yl)triimidazo[1,2-a:1',2'-c:1",2"-e][1,3,5]triazine-3,7-dicarbaldehyde **$(CHO)_2$TTPyr**

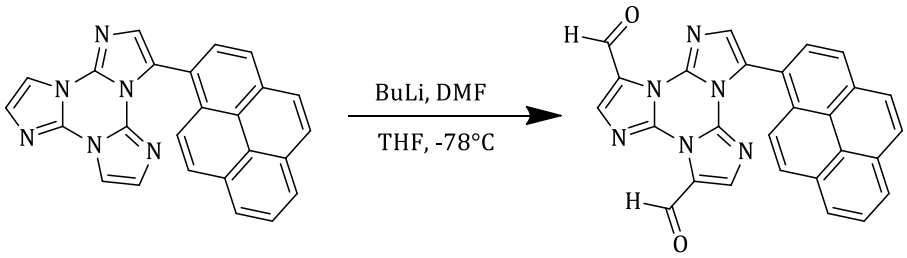

$(CHO)_2$TTPyr was prepared by lithiation of **TTPyr** with *n*-butyllithium followed by nucleophilic addition on dimethylformamide. In a typical reaction, **TTPyr** (200 mg, 0.50 mmol) was dissolved in anhydrous THF (45 mL) in a round-bottom flask under nitrogen atmosphere. The system was cooled at -78 °C, then *n*-BuLi 2.5 M in hexane (450 μL, 1.13 mmol) was added. The formation of a carbanionic species was evident from the appearance of an intense red colour. After 1h, anhydrous DMF (1 mL, 12.93 mmol) was added at -78 °C and the reaction mixture stirred overnight under static nitrogen up to room temperature. Then the reaction was added with an ammonium chloride saturated solution (2 mL) and stirred for 30 minutes. The reaction crude was evaporated to dryness and purified

by DCM/H_2O extraction. The combined organic phases were dried over Na_2SO_4 and filtered. The filtrate was evaporated to dryness to afford a solid which was further purified by automated flash chromatography on SiO_2 with DCM/ACN as eluents to give the product as a yellow powder (87 mg; yield 38%; R_f 0.79 in DCM/ACN = 8:2). Before performing spectroscopic measurements, the product has been crystallized by slow evaporation from DCM solutions affording a yellow solid.
NMR data (9,4 T, DMSO-d_6, 298 K, δ, ppm): ^{1}H-NMR 10.98 (1H, s), 10.73 (1H, s), 8.44-8.06 (10H, m), 7.73 (2H, s); ^{13}C-NMR {^{1}H} 180.4, 179.9, 140.0, 138.6, 136.7, 135.6, 135.4, 131.8, 130.6, 130.7, 130.3, 129.9, 129.5, 128.4, 128.1, 128.0, 127.6, 127.3, 126.5, 125.9, 125.8, 125.7, 125.2, 124.3, 123.7, 123.6, 122.3.
MS (ESI-positive ion mode): m/z: 455 $[M+H]^+$.

4.3. Computational details

DFT and TDDFT calculations on **(CHO)$_2$TTPyr** were performed with Gaussian 16 program (Revision A.03) [48] adopting the same ωB97X/6-311++G(d,p) protocol as used for previous calculations on the full series of **TT** derivatives [11–20], including in particular **TTPyr** [20]. The ωB97X functional [49] was chosen owing to its ability in correctly treating at the same time not only ground and excited states properties, but also π-π stacking interactions which are of great importance to interpret the multi-faceted emissive properties of this family of compounds. The geometry of **(CHO)$_2$TTPyr** was optimized in both DMSO and toluene starting from the X-ray RT conformation previously obtained for **TTPyr** [20] and properly adding the two CHO fragments. The Polarized Continuum Model in its integral equation formalism (IEFPCM) [50] was used to describe the solvent effect.

4.4. Crystal Structure Analysis

Single-crystal X-ray diffraction data for **TTPyr**/PA, were collected at room temperature on a Bruker APEX II CCD area detector diffractometer, using graphite-monochromated Mo Kα radiation (λ = 0.71073 Å). A full sphere of reciprocal space was scanned by 0.5° ω steps, collecting 2160 frames in six different regions of the reciprocal space. After integration, an empirical absorption correction was made on the basis of the symmetry-equivalent reflection intensities measured [51].
The structure was solved by direct methods (SIR2014) [52] and subsequent Fourier synthesis; then was refined by full-matrix least-squares on F^2 (SHELX 2014) [53] using all reflections. Weights were assigned to individual observations according to the formula $w = 1/[\sigma 2(F_o^2) + (aP)^2 + bP]$, where $P = (F_o^2 + 2F_c^2)/3$; *a* and *b* were chosen to give a flat analysis of variance in terms of F_o^2. Anisotropic parameters were assigned to all non-hydrogen atoms. All the hydrogen atoms were clearly visible in Difference-Fourier maps, however, they were eventually placed in idealized position and refined riding on their parent atom with an isotropic displacement parameter 1.2 (or 1.5) times that of the pertinent parent atom. The position of the hydroxyl hydrogen of the picric acid was refined. Its refined position is in agreement with the formation of a bifurcated hydrogen bond with O2 and N12.
Residual electron density peaks and holes are low, randomly distributed in the asymmetric unit and do not have any chemical significance.
The collected dataset shows some problematic features, as testified by the higher than usual values of R_{int} and R_σ (0.107, and 0.176, respectively). These finding can be safely attributed to the poor diffraction power of this co-crystal as confirmed by similar datasets collected for many different specimens from different crystallization batches.
CCDC 2192407 contain the supplementary crystallographic data for **TTPyr**/PA. These data can be obtained free of charge from the Cambridge Crystallographic Data Centre http://www.ccdc.cam.ac.uk/conts/retrieving.html.

5. Declaration of Competing Interest

The authors declare that they have no known competing financial interests or personal relationships that could have appeared to influence the work reported in this paper.

6. Acknowledgements

This research is part of the project "One Health Action Hub: University Task Force for the resilience of territorial ecosystems", Supported by Università degli Studi di Milano – PSR 2021 - GSA - Linea 6. The use of instrumentation purchased through the Regione Lombardia-Fondazione Cariplo joint SmartMatLab Project is gratefully acknowledged. Pierluigi Mercandelli is acknowledged for X-Ray diffraction data analysis.

References

[1] Barnes BB, Snow NH. Recent Advances in Sample Preparation for Explosives. Comprehensive Sampling and Sample Preparation, Elsevier; 2012, p. 893–926. https://doi.org/10.1016/B978-0-12-381373-2.00119-8.

[2] Yinon J. Toxicity and Metabolism of Explosives. vol. 1. CRC Press: Boca Raton (FL, USA); 1990.

[3] Dong W, Ma Q, Ma Z, Duan Q, Lü X, Qiu N, et al. Phosphorescent iridium(III) complex based photoluminescence sensor for sensitive and selective detection of picric acid. Dyes Pigm. 2020;172. https://doi.org/10.1016/J.DYEPIG.2019.107799.

[4] Prusti B, Chakravarty M. An electron-rich small AIEgen as a solid platform for the selective and ultrasensitive on-site visual detection of TNT in the solid, solution and vapor states. Analyst 2020;145:1687–94. https://doi.org/10.1039/C9AN02334H.

[5] Fan YZ, Tang Q, Liu SG, Yang YZ, Ju YJ, Xiao N, et al. A smartphone-integrated dual-mode nanosensor based on novel green-fluorescent carbon quantum dots for rapid and highly selective detection of 2,4,6-trinitrophenol and pH. Appl. Surf. Sci. 2019;492:550–7. https://doi.org/10.1016/J.APSUSC.2019.06.224.

[6] Wang X, Zhang X, Cao H, Huang Y. A facile and rapid approach to synthesize uric acid-capped Ti3C2 MXene quantum dots for the sensitive determination of 2,4,6-trinitrophenol both on surfaces and in solution. J. Mater. Chem. B 2020;8:10837–44. https://doi.org/10.1039/D0TB02078H.

[7] Nagarkar SS, Desai A v., Ghosh SK. A fluorescent metal–organic framework for highly selective detection of nitro explosives in the aqueous phase. Chem. Commun. 2014;50:8915–8. https://doi.org/10.1039/C4CC03053B.

[8] Sun X, Wang Y, Lei Y. Fluorescence based explosive detection: From mechanisms to sensory materials. Chem. Soc. Rev. 2015;44:8019–61. https://doi.org/10.1039/c5cs00496a.

[9] Germain ME, Knapp MJ. Optical explosives detection: from color changes to fluorescence turn-on. Chem. Soc. Rev. 2009;38:2543. https://doi.org/10.1039/b809631g.

[10] Mei J, Leung NLC, Kwok RTK, Lam JWY, Tang BZ. Aggregation-Induced Emission: Together We Shine, United We Soar! Chem. Rev. 2015;115:11718–940. https://doi.org/10.1021/acs.chemrev.5b00263.

[11] Forni A, Lucenti E, Botta C, Cariati E. Metal free room temperature phosphorescence from molecular self-interactions in the solid state. J. Mater. Chem. C 2018;6:4603–26. https://doi.org/10.1039/c8tc01007b.

[12] Lucenti E, Forni A, Botta C, Carlucci L, Giannini C, Marinotto D, et al. H-Aggregates Granting Crystallization-Induced Emissive Behavior and Ultralong Phosphorescence from a Pure Organic Molecule. J. Phys. Chem. Lett. 2017;8:1894–8. https://doi.org/10.1021/acs.jpclett.7b00503.

[13] Previtali A, Lucenti E, Forni A, Mauri L, Botta C, Giannini C, et al. Solid State Room Temperature Dual Phosphorescence from 3-(2-Fluoropyridin-4-yl)triimidazo[1,2-*a*:1′,2′-*c*:1″,2″-*e*][1,3,5]triazine. Molecules 2019, Vol 24, Page 2552 2019;24:2552. https://doi.org/10.3390/MOLECULES24142552.

[14] Lucenti E, Forni A, Previtali A, Marinotto D, Malpicci D, Righetto S, et al. Unravelling the intricate photophysical behavior of 3-(pyridin-2-yl)triimidazotriazine AIE and RTP polymorphs. Chem. Sci. 2020;11:7599–608. https://doi.org/10.1039/D0SC02459G.

[15] Giannini C, Forni A, Malpicci D, Lucenti E, Marinotto D, Previtali A, et al. Room temperature phosphorescence from organic materials: Unravelling the emissive behaviour of chloro-substituted derivatives of cyclic triimidazole. Eur. J. Org. Chem. 2021;2021:2041–9. https://doi.org/10.1002/ejoc.202100131.

[16] Malpicci D, Giannini C, Lucenti E, Forni A, Marinotto D, Cariati E. Mono-, Di-, Tri-Pyrene Substituted Cyclic Triimidazole: A Family of Highly Emissive and RTP Chromophores. Photochem 2021;1:477–87. https://doi.org/10.3390/photochem1030031.

[17] Lucenti E, Forni A, Botta C, Carlucci L, Colombo A, Giannini C, et al. The effect of bromo substituents on the multifaceted emissive and crystal-packing features of cyclic triimidazole derivatives. ChemPhotoChem 2018;2:801–5. https://doi.org/10.1002/cptc.201800151.

[18] Lucenti E, Forni A, Botta C, Giannini C, Malpicci D, Marinotto D, et al. Intrinsic and Extrinsic Heavy-Atom Effects on the Multifaceted Emissive Behavior of Cyclic Triimidazole. Chem. Eur. J. 2019;25:2452–6. https://doi.org/10.1002/chem.201804980.

[19] Lucenti E, Forni A, Botta C, Carlucci L, Giannini C, Marinotto D, et al. Cyclic Triimidazole Derivatives: Intriguing Examples of Multiple Emissions and Ultralong Phosphorescence at Room Temperature. Angew. Chem. Int. Ed. 2017,56,16302–16307. https://doi.org/10.1002/ange.201710279.

[20] Previtali A, He W, Forni A, Malpicci D, Lucenti E, Marinotto D, et al. Tunable Linear and Nonlinear Optical Properties from Room Temperature Phosphorescent Cyclic Triimidazole-Pyrene Bio-Probe. Chem. Eur. J. 2021;27:16690–700. https://doi.org/10.1002/CHEM.202102839.

[21] Lucenti E, Cariati E, Previtali A, Marinotto D, Forni A, Bold V, et al. Versatility of Cyclic Triimidazole to Assemble 1D, 2D, and 3D Cu(I) Halide Coordination Networks. Cryst. Growth Des. 2019;19:1567–75. https://doi.org/10.1021/acs.cgd.8b01199.

[22] Malpicci D, Lucenti E, Forni A, Marinotto D, Previtali A, Carlucci L, et al. Ag(I) and Cu(I) cyclic-triimidazole coordination polymers: revealing different deactivation channels for multiple room temperature phosphorescences. Inorg. Chem. Front. 2021;8:1312–23. https://doi.org/10.1039/D0QI01377C.

[23] Melnic E, Kravtsov VCh, Lucenti E, Cariati E, Forni A, Siminel N, et al. Regulation of π···π stacking interactions between triimidazole luminophores and comprehensive emission quenching by coordination to Cu(II). New J. Chem. 2021;45:9040–52. https://doi.org/10.1039/D1NJ00909E.

[24] Shanmugaraju S, Mukherjee PS. π-Electron rich small molecule sensors for the recognition of nitroaromatics. Chem. Commun. 2015;51:16014–32. https://doi.org/10.1039/C5CC07513K.
[25] Singla P, Kaur P, Singh K. Discrimination in excimer emission quenching of pyrene by nitroaromatics. Tetrahedron Lett. 2015;56:2311–4. https://doi.org/10.1016/J.TETLET.2015.03.053.
[26] Sriyab S, Jorn-Iat K, Prompinit P, Wolschann P, Hannongbua S, Suramitr S. Photophysical properties of 1-pyrene-based derivatives for nitroaromatic explosives detection: Experimental and theoretical studies. J. Lumin. 2018;203:492–9. https://doi.org/10.1016/J.JLUMIN.2018.06.070.
[27] Neupane U, Rai RN. Solid state synthesis of novel charge transfer complex and studies of its crystal structure and optical properties. J. Solid State Chem. 2018;268:67–74. https://doi.org/10.1016/J.JSSC.2018.08.029.
[28] Ardic Alidagi H, Tümay SO, Şenocak A, Çiftbudak ÖF, Çoşut B, Yeşilot S. Constitutional isomers of dendrimer-like pyrene substituted cyclotriphosphazenes: synthesis, theoretical calculations, and use as fluorescence receptors for the detection of explosive nitroaromatics. New J. Chem. 2019;43:16738–47. https://doi.org/10.1039/C9NJ03695D.
[29] Kim SY, Kim MJ, Ahn M, Lee KM, Wee KR. Systematic energy band gap control of pyrene based donor-acceptor-donor molecules for efficient chemosensor. Dyes Pigm. 2021;191:109362. https://doi.org/10.1016/J.DYEPIG.2021.109362.
[30] Khasanov AF, Kopchuk DS, Kovalev IS, Taniya OS, Giri K, Slepukhin PA, et al. Extended cavity pyrene-based iptycenes for the turn-off fluorescence detection of RDX and common nitroaromatic explosives. New J. Chem. 2017;41:2309–20. https://doi.org/10.1039/C6NJ02956F.
[31] Mosca L, Karimi Behzad S, Anzenbacher P. Small-Molecule Turn-On Fluorescent Probes for RDX. J. Am. Chem. Soc. 2015;137:7967–9. https://doi.org/10.1021/JACS.5B04643.
[32] Kovalev IS, Taniya OS, Kopchuk DS, Giri K, Mukherjee A, Santra S, et al. 1-Hydroxypyrene-based micelle-forming sensors for the visual detection of RDX/TNG/PETN-based bomb plots in water. New J. Chem. 2018;42:19864–71. https://doi.org/10.1039/C8NJ03807D.
[33] Kovalev IS, Taniya OS, Sadieva LK, Volkova NN, Minin AS, Grzhegorzhevskii K v., et al. Bola-type PAH-based fluorophores/chemosensors: Synthesis via an unusual clemmensen reduction and photophysical studies. J. Photochem. Photobiol. A 2021;420:113466. https://doi.org/10.1016/J.JPHOTOCHEM.2021.113466.
[34] He G, Yan N, Yang J, Wang H, Ding L, Yin S, et al. Pyrene-containing conjugated polymer-based fluorescent films for highly sensitive and selective sensing of TNT in aqueous medium. Macromolecules 2011;44:4759–66. https://doi.org/10.1021/MA200953S/SUPPL_FILE/MA200953S_SI_001.PDF.
[35] Zhang C, Pan X, Cheng S, Xie A, Dong W. Pyrene Derived aggregation-induced emission sensor for highly selective detection of explosive CL-20. J. Lumin. 2021;233:117871. https://doi.org/10.1016/J.JLUMIN.2020.117871.
[36] Panigrahi A, Sahu BP, Mandani S, Nayak D, Giri S, Sarma TK. AIE active fluorescent organic nanoaggregates for selective detection of phenolic-nitroaromatic explosives and cell imaging. J. Photochem. Photobiol. A 2019;374:194–205. https://doi.org/10.1016/J.JPHOTOCHEM.2019.01.029.

[37] Islam ASM, Sasmal M, Maiti D, Dutta A, Show B, Ali M. Design of a Pyrene Scaffold Multifunctional Material: Real-Time Turn-On Chemosensor for Nitric Oxide, AIEE Behavior, and Detection of TNP Explosive. ACS Omega 2018;3:10306–16. https://doi.org/10.1021/ACSOMEGA.8B01294/SUPPL_FILE/AO8B01294_SI_001.PDF.

[38] Gole B, Song W, Lackinger M, Mukherjee PS. Explosives sensing by using electron-rich supramolecular polymers: Role of intermolecular hydrogen bonding in significant enhancement of sensitivity. Chem. Eur. J. 2014;20:13662–80. https://doi.org/10.1002/CHEM.201403345.

[39] Yang XL, Hu DY, Chen Q, Li L, Li PX, Ren S bin, et al. A pyrene-cored conjugated microporous polycarbazole for sensitive and selective detection of hazardous explosives. Inorg. Chem. Commun. 2019;107:107453. https://doi.org/10.1016/J.INOCHE.2019.107453.

[40] Lin G, Ding H, Yuan D, Wang B, Wang C. A Pyrene-Based, Fluorescent Three-Dimensional Covalent Organic Framework. J. Am. Chem. Soc. 2016;138:3302–5. https://doi.org/10.1021/JACS.6B00652/SUPPL_FILE/JA6B00652_SI_001.PDF.

[41] Mondal T, Mondal I, Biswas S, Mane M v., Panja SS. Mechanistic Insight into Selective Sensing of Hazardous Hg2+ and Explosive Picric Acid by Using a Pyrene-Azine-Hydroxyquinoline Framework in Differential Media. ChemistrySelect 2020;5:9336–49. https://doi.org/10.1002/SLCT.202001798.

[42] Lu S, Fan W, Liu H, Gong L, Xiang Z, Wang H, et al. Four imidazole derivative AIEE luminophores: sensitive detection of NAC explosives. New J. Chem. 2021;45:6889–94. https://doi.org/10.1039/D0NJ06007K.

[43] Zhou JJ, Xu W, Xiao JY, Hu XG, Xiao HP, Liu BL. A stable 3-D Cd(II) metal–organic framework formed by aromatic carboxylate and flexible imidazole ligand for sensing of nitroaromatic explosives. J. Coord. Chem. 2021;74:1856–65. https://doi.org/10.1080/00958972.2021.1935903.

[44] Shrivastava A, Gupta V. Methods for the determination of limit of detection and limit of quantitation of the analytical methods. Chron. Young Sci. 2011;2:21. https://doi.org/10.4103/2229-5186.79345.

[45] Senthilvelan A, Ho IT, Chang KC, Lee GH, Liu YH, Chung WS. Cooperative recognition of a copper cation and anion by a calix[4]arene substituted at the lower rim by a ß-amino-a,ß-unsaturated ketone. Chem. Eur. J. 2009;15:6152–60. https://doi.org/10.1002/CHEM.200802654.

[46] Schubert DM, Natan DT, Wilson DC, Hardcastle KI. Facile Synthesis and Structures of Cyclic Triimidazole and Its Boric Acid Adduct. Cryst. Growth Des. 2011;11:843–50. https://doi.org/10.1021/cg101489t.

[47] Taylor CA, Rinkenbach WmH. The Solubility of Trinitrotoluene in Organic Solvents. J. Am. Chem. Soc. 1922;45:44–59. https://doi.org/10.1021/ja01654a006.

[48] M. J. Frisch, G. W. Trucks, H. B. Schlegel, G. E. Scuseria, M. A. Robb, J. R. Cheeseman, et al. Gaussian 16 2016.

[49] Chai J-D, Head-Gordon M. Long-range corrected hybrid density functionals with damped atom–atom dispersion corrections. Phys. Chem. Chem. Phys. 2008;10:6615. https://doi.org/10.1039/b810189b.

[50] Scalmani G, Frisch MJ. Continuous surface charge polarizable continuum models of solvation. I. General formalism. J. Chem. Phys. 2010;132:114110. https://doi.org/10.1063/1.3359469.

[51] SADABS 2012. Area detector absorption correction. Bruker AXS Inc., Madison, Wisconsin, USA n.d.
[52] Burla MC, Caliandro R, Carrozzini B, Cascarano GL, Cuocci C, Giacovazzo C, et al. Crystal structure determination and refinement via SIR2014. J. Appl. Crystallogr. 2015;48:306–9. https://doi.org/10.1107/S1600576715001132.
[53] Sheldrick GM, IUCr. Crystal structure refinement with SHELXL. Urn:Issn:2053-2296 2015;71:3–8. https://doi.org/10.1107/S2053229614024218.

Highlights

- Two pyrene-susbstituted cyclic triimidazoles exhibit selective detection of nitroaromatic energetic compounds.
- Time resolved experiments revealed static quenching mechanism with formation of a ground state complex.
- X-Ray diffraction analysis of the dark complex with picric acid is performed.

Declaration of Competing Interest

The authors declare that they have no known competing financial interests or personal relationships that could have appeared to influence the work reported in this paper.